Journal of Energy Storage 179 (2026) 123987

Contents lists available at ScienceDirect

Journal of Energy Storage

journal homepage: www.elsevier.com/locate/est

Research Papers

In-Situ anchoring of amorphous Ni_xB nanoparticles onto Nb_2CT_x MXene nanosheets for high-performance asymmetric supercapacitors

Ramaraj Sukanya [a,1], Raj Karthik [a,b,1], Chelladurai Karuppiah [c,d], Deivasigamani Ranjith Kumar [e], Milton Ahamed [b], Hye Jin Lee [c], Carmel B. Breslin [a,*], Jae-Jin Shim [b,*]

[a] Department of Chemistry, Maynooth University, Maynooth, Co. Kildare, Ireland
[b] School of Chemical Engineering, Yeungnam University, 280 Daehak-ro, Gyeongsan, Gyeongbuk, 38541, Republic of Korea
[c] Department of Chemistry and Green-Nano Materials Research Center, Kyungpook National University, 80, Daehak-ro, Buk-gu, Daegu City, 41566, Republic of Korea
[d] Institute for Basic Science Convergence, Kyungpook National University, 80, Daehak-ro, Buk-gu, Daegu City, 41566, Republic of Korea
[e] Centre for Organic and Nanohybrid Electronics, Silesian University of Technology, Konarskiego 22B, 44-100 Gliwice, Poland

ARTICLE INFO

Keywords:
Niobium carbide MXene
Metal boride
Carbon cloth
Reduced graphene oxide
Asymmetric device
Supercapacitors

ABSTRACT

An amorphous nickel boride/niobium carbide MXene (Ni_xB/Nb_2CT_x) composite was designed and synthesized via a combined HF-assisted etching and in-situ chemical reduction strategy. The uniform anchoring of 0D Ni_xB nanoparticles within the multilayered Nb_2CT_x nanosheets led to the formation of a robust composite with favorable interfacial interactions, abundant active sites, and improved charge transport pathways. The composite was directly coated on carbon cloth, which served as a flexible and conductive substrate to ensure efficient electron collection and mechanical stability of the electrode, while not contributing to electrochemical capacitance. Detailed structural and electrochemical analyses indicate that the integration of Ni_xB with Nb_2CT_x influences the electronic environment, improves redox activity, and promotes ion diffusion, thereby contributing to enhanced charge storage kinetics. Among the as-prepared samples, the optimized Ni_xB/Nb_2CT_x-50 electrode delivers a specific capacitance of 606.7 F g^{-1} at 1 A g^{-1}, demonstrating a moderate rate capability with a capacitance retention of 43.2% from 1 to 20 A g^{-1}. Furthermore, an asymmetric supercapacitor assembled with Ni_xB/Nb_2CT_x-50 and reduced graphene oxide (rGO) electrodes achieved a remarkable energy density of 46.7 Wh kg^{-1} at a power density of 825 W kg^{-1}. This work provides new insights into the interfacial engineering of amorphous transition metal boride-MXene hybrids toward next-generation high energy density supercapacitor applications.

1. Introduction

The overutilization and exploitation of human energy sources, especially fossil fuels, have led to a rise in global warming issues. Finding an alternative, clean, and sustainable energy source, such as renewable energy, is an efficient way to address the escalating energy crisis. At the same time, these kinds of energy sources are intermittent and are converted into electrical energy for utilization and transmission purposes [1–3]. Therefore, it is essential to develop a clean energy storage and conversion device to overcome the energy scarcity problem. Recently, electrochemical energy storage (EES), such as supercapacitors (SCs), has been proven as a sustainable energy storage system that provides solutions to energy shortages with its high energy and power densities [4,5]. Moreover, the SCs exhibit fast charge-discharge cycling but can operate only for a shorter period because of the rapid non-faradaic process [6,7]. The practical application of SCs is limited due to their lower energy density compared to batteries. To improve the energy density of SCs, the development of battery-type SCs that combine the advantages of both faradaic and EDLC behavior have been developed. For this purpose, new electrode materials with a large contactable specific surface area and high conductivity, as well as the use of high operating voltage window electrolytes are key factors in developing high performance battery-type SCs [8]. Recently, two-dimensional (2D) metal carbides such as MXenes have attracted significant attention for

* Corresponding authors.
E-mail addresses: Carmel.Breslin@mu.ie (C.B. Breslin), jjshim@yu.ac.kr (J.-J. Shim).
[1] The authors R. Sukanya, and R. Karthik equally contributed to this manuscript.

https://doi.org/10.1016/j.est.2026.123987
Received 5 February 2026; Received in revised form 25 July 2026; Accepted 31 July 2026
Available online 7 August 2026

their usage as efficient EES electrodes in terms of their remarkable properties, including intrinsic high metallic conductivity, hydrophilic-fast ion diffusion capability and favorable pseudo-capacitive nature [9,10]. Among the MXene family, niobium-based MXenes have not yet been widely investigated for SCs due to their more complex synthesis process compared to other MXenes. This M_2X-type Nb_2CT_x MXene exhibits higher areal and gravimetric capacitance than the traditional Ti_3C_2 MXene [11]. The higher oxidation states of Nb_2CT_x provide more redox-active Nb sites on the layer surface for the intercalation/deintercalation of ions, thereby enhancing the faradaic contribution and resulting in higher specific capacitance during long-term charging/discharging [12]. On the other hand, the Nb_2CT_x MXene exhibits high electrical conductivity, which accelerates charge adsorption and desorption, and thereby amplifies the ion diffusion rate. Additionally, its heightened electrochemical behavior fosters swift and reversible faradaic redox reactions at the electrode surface, thereby enabling charge storage in SCs. However, the pristine Nb_2CT_x MXene exhibits layer restacking and spontaneous aggregation phenomena, which can be initiated by van der Waals interactions between layers [13,14]. This phenomenon leads to the blockage of ion transport channels and reduces the surface interaction between the Nb active sites and electrolyte ions, which inhibits the long-time energy storage process by diminishing the structural stability [13]. This could be effectively countered by the introduction of another nanostructure (0D/1D/2D) to form multidimensional heterointerfaces/composites [15,16]. Multi-dimensional structures provide high surface area and enhance structural and electronic properties by incorporating individual component features, which may result in higher capacitance and improved mechanical stability. Compared to 1D and 2D structures, the combination of 2D MXene with 0D nanoparticles avoids self-accumulation of layers and helps to improve the intercalation/deintercalation of ions, thereby improving charge/discharge. Not only does the 0D, 2D layer structure significantly shorten the ion diffusion and charge-transfer paths, but it also provides buffer space for volume changes during charging and discharging. On this basis, *Shen* et al. [17] reported the combination of self-assembled Co_3O_4/Nb_2CT_x and achieved a specific capacitance of up to 1061 F g^{-1} at the current density of 2 A g^{-1}. This emphasizes the benefits of multi-dimensional structures, which help enhance the electrochemical performance of both materials.

According to recent studies, transition metal borides (TMBs) are considered a well-known SC electrode material due to their unique electronic and metallic bonding properties. Among their remarkable properties, the metallic conductivity, high *d*-electron densities, and active unsaturated sites are the most promising features for their enhanced electrochemical performance [18]. Especially, nickel-containing metalloids such as nickel borides (NiB, Ni_xB, Ni_2B and Ni_3B) show high theoretical capacity, making them highly suitable for SC fabrication [19,20]. In addition, the presence of electron-deficient boron (B) and nickel (Ni) offers a unique advantage in the fabrication of electrodes, which helps to affect the electron distribution around the whole system, thereby promoting the transport of OH^- ions during the electrochemical storage process [15]. This remarkable storage mechanism results from their amorphous nature, which features a disordered atomic arrangement and exhibits unsaturated active sites that help to improve the redox reaction during the charge/discharge process. However, it should be highlighted that pure Ni_xB particles are relatively unstable and easily aggregated during the long-time cycles, which results in a reduction in capacitance and cyclic stability [21,22]. Therefore, the construction of different-dimensional structures was introduced to overcome this disadvantage of pristine Ni_xB. In particular, the presence of a close contact structure combination (0D/2D) can tailor their physical/chemical features and facilitate ion/electron transport at the electrode interface, resulting in enhanced energy storage capability and remarkable cycle stability across various electrolyte media. According to previous reports [23], the combination of 2D MXene with 0D metal boride can help mitigate the individual drawbacks of each material, such as restacking and aggregation. This hybrid configuration enables complementary advantages, including improved energy storage performance and enhanced structural stability of the overall system through favorable interfacial interactions.

Inspired by these considerations, a composite comprising exfoliated 2D Nb_2CT_x with well-decorated Ni_xB nanoparticles was developed by HF etching and in-situ chemical reduction. The effects of the etching conditions and the incorporation of Ni_xB on the structural features and electrochemical activity of Nb_2CT_x MXene were systematically evaluated. Characterization results indicate favorable interactions between Nb_2CT_x and Ni_xB, suggesting strong interfacial coupling between the two phases, which contributes to the enhanced electrochemical response. The electrochemical performance of the Ni_xB/Nb_2CT_x composite, including its specific capacitance was assessed using cyclic voltammetry, galvanostatic charge-discharge, and electrochemical impedance spectroscopy. In addition, the concentrations of Nb_2CT_x MXene in the Ni_xB/Nb_2CT_x composite were systematically varied to elucidate its influence on charge-storage behavior and to optimize the material for SC fabrication. Guided by these optimization studies, an asymmetric SC device was constructed using Ni_xB/Nb_2CT_x and rGO electrodes (Ni_xB/Nb_2CT_x//rGO), demonstrating high energy density and power density performance.

2. Experimental section

Comprehensive details regarding the chemicals and reagents used, characterization techniques, and electrochemical testing procedures are provided in the Supporting Information (section S2.1-S2.3).

2.1. Preparation of amorphous nickel boride (Ni_xB)

Amorphous Ni_xB was synthesized via a chemical reduction method [15,23]. Initially, 0.742 g of $NiCl_2$ was dissolved in 25 mL of deionized (DI) water under continuous stirring for 10 min to obtain solution A. In a separate beaker, 0.189 g of $NaBH_4$ and 0.04 g of NaOH were dissolved in 10 mL of DI water to form solution B. Afterwards, solution A was placed in an ice-bath maintained at 0 °C and purged with N_2 gas for 15 min to create an inert atmosphere. Subsequently, solution B was slowly added dropwise to solution A using a syringe. The addition of $NaBH_4$ initiated vigorous gas evolution, and a black precipitate formed, confirming the reduction. The reaction was maintained for 30 min under continuous stirring in an ice-bath and N_2 flow. The resulting precipitate was collected by centrifugation, washed repeatedly with DI water and ethanol, and then dried overnight in a vacuum oven at 50 °C. The dried amorphous Ni_xB powder was stored in a sealed vial for subsequent use.

2.2. Preparation of Nb_2CT_x MXene from Nb_2AlC MAX phase

The synthesis of Nb_2CT_x MXene was carried out following our previously reported method [45]. Briefly, the 2D Nb_2CT_x MXene was synthesized through a selective HF etching process. In a typical procedure, 50 mL of HF solution was carefully poured into a 100 mL PTFE container, and 0.5 g of Nb_2AlC powder was slowly introduced into the acid under stirring. The etching reaction was carried out at 60 °C for 120 h while maintaining a stirring rate of 600 rpm. After etching, the suspension was repeatedly washed with DI water via centrifugation until the pH of the supernatant reached approximately 6-7. Finally, the resulting MXene was freeze-dried and stored in an airtight container. An overall schematic illustration of the synthesis process of amorphous Ni_xB, Nb_2CT_x MXene and Ni_xB/Nb_2CT_x composites is depicted in Scheme 1.

2.3. Preparation of amorphous Ni_xB/Nb_2CT_x composites

To prepare the Ni_xB/Nb_2CT_x composite, 50 mg of Nb_2CT_x powder was first dispersed in 25 mL of DI water and ultrasonicated for 30 min to

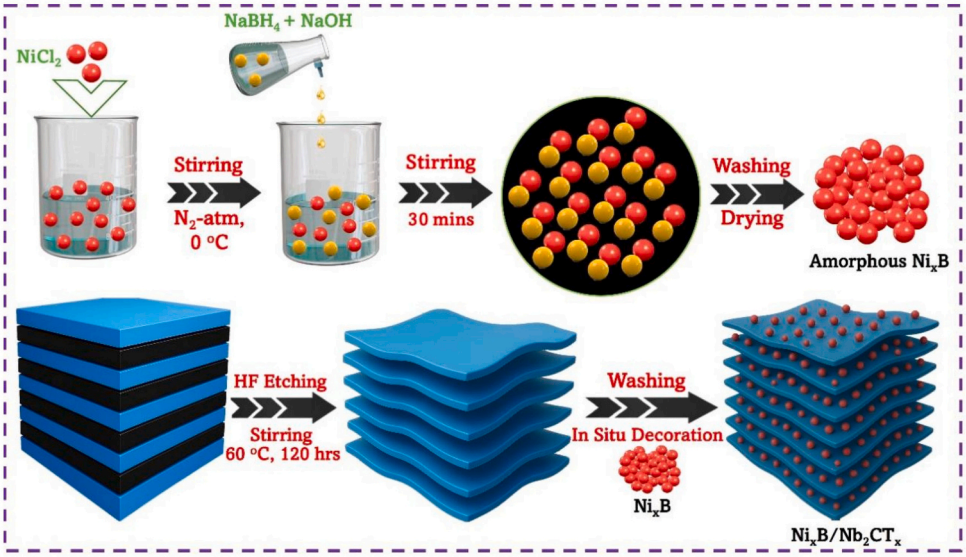

Scheme 1. Schematic representation of the synthesis of amorphous Ni_xB, Nb_2CT_x MXene, and Ni_xB/Nb_2CT_x composites.

achieve a uniform suspension. The in-situ deposition of amorphous Ni_xB onto the MXene surface was then performed following the same reduction process described in Section 2.1. The composite formation involved the simultaneous reduction of Ni^{2+} ions and incorporation of boron species onto the Nb_2CT_x sheets, resulting in a uniform Ni_xB coating. The obtained materials were labelled as Ni_xB/Nb_2CT_x-50, dried under vacuum at 50 °C overnight, and stored in airtight containers. For comparative purposes, the initial amount of Nb_2CT_x was varied (25, 50, and 150 mg), and the corresponding products were denoted as Ni_xB/Nb_2CT_x-25, Ni_xB/Nb_2CT_x-50, and Ni_xB/Nb_2CT_x-150, respectively.

3. Results and discussion

The preparation of multilayers of Nb_2CT_x from the MAX phase (Nb_2AlC) and the decoration of Ni_xB on Nb_2CT_x were carried out through multiple steps of the synthesis process, as illustrated in Scheme 1. Initially, the multilayer Nb_2CT_x MXene was synthesized through the Al etching process using HF as a fluoride-based etchant. The MAX phase is treated with HF, and exfoliation occurs via an in-situ reaction. During this process, F^- ions are intercalated into the dense surface of the Nb_2AlC, facilitating the conversion to multi-layered Nb_2CT_x MXene. After several washes with water, the removal of the upper solution produces pure multilayer Nb_2CT_x MXene. After etching and washing, the surface of Nb_2CT_x is modified with functional groups such as —F and —O. Due to the presence of these functional groups, the Nb_2CT_x MXene surface becomes negatively charged, leading to electrostatic repulsion between the layers. Following the surface charge modification, the in-situ growth of Ni_xB was carried out by introducing Ni^{2+} ions into an aqueous solution of Nb_2CT_x. Subsequently, $NaBH_4$ was slowly added to the solution under continuous N_2 gas purging. During the in-situ reaction, the positively charged Ni^{2+} ions react with $NaBH_4$, leading to the integration of Ni_xB onto the surface of Nb_2CT_x MXene through the creation of a strong electrostatic interaction between both components.

Before the electrochemical testing, the preliminary physicochemical properties of the prepared Nb_2CT_x MXene and Ni_xB/Nb_2CT_x composite were assessed using various characterization techniques, such as thin film XRD, FE-SEM, EDAX, and XPS. Fig. 1 shows the XRD patterns of Nb_2CT_x MXene (Fig. 1(a)), Ni_xB (Fig. 1(b)), and the Ni_xB/Nb_2CT_x composites (Figs. 1(c-e)). In agreement with previous reports, the XRD pattern of Nb_2AlC shows major peaks at angles of 12.7°, 25.7°, 33.3°, 33.9°, 38.7°, 42.7°, 52.1°, 57.8°, 59.5°, corresponding to the planes (002), (004), (100), (101), (103), (104), (106), (107), and (110),

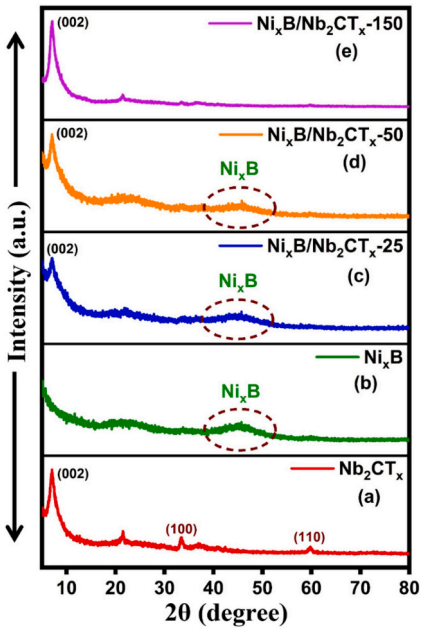

Fig. 1. Thin film-XRD patterns of (a) Nb_2CT_x MXene, (b) Ni_xB, (c) Ni_xB/Nb_2CT_x-25, (d) Ni_xB/Nb_2CT_x-50, and (e) Ni_xB/Nb_2CT_x-150 composites. The XRD pattern of Ni_xB (b) is adapted from our previous work [23].

respectively [24,45]. After exfoliation with HF (Fig. 1(a)), the peak shifts from 12.7° to a lower angle of 6.96°, indicating the successful etching out of Al from the Nb_2AlC by —F and —O functional groups [25]. Additionally, the expansion of the lattice parameter indicates enhanced interlayer spacing in Nb_2CT_x MXene compared to the previously reported Nb_2AlC [24]. Notably, the peaks at 33.4° and 59.5° corresponding to the (100) and (110) planes of the MAX phase are still observed in the exfoliated Nb_2CT_x, indicating partial retention of the in-plane ordering after HF treatment, which is commonly reported in multilayer MXene systems [45]. Furthermore, a peak at 21.5° is observed in the Nb_2CT_x pattern, which is attributed to niobium oxide (Nb_xO_y). This oxide phase likely forms during the HF etching process due to partial surface oxidation of Nb upon exposure to moisture and oxygen, a phenomenon commonly observed in Nb-based MXene systems during acid treatment and subsequent handling. The XRD analysis

clearly shows that the etching with HF introduces F^- ions between the layers, helping to expose Nb and additional groups, which results in enhanced interlayer spacing. However, the presence of a small and negligible peak at 41.0° suggests the existence of a small amount of unreacted Al in the Nb_2AlC phase. Compared to reported MAX phases, the intensity of the main peak is much reduced and weakened, indicating that the prepared Nb_2CT_x MXene is in the form of multilayers and confirming the successful formation of MXene from the stacked MAX phase. Moreover, the increased d-spacing value also indicates an increase in the surface area and active sites on the layered structure. The larger interlayer spacing of Nb_2CT_x facilitates faster ion adsorption and intercalation, improving ion diffusion and charge transport at the electrode-electrolyte interface, thereby resulting in enhanced electrochemical performance. The XRD patterns for the Ni_xB/Nb_2CT_x composites are shown in Fig. 1(c-e), providing evidence of the presence of both materials in the composite. The XRD pattern of Ni_xB/Nb_2CT_x shows both sharper (6.96°) and broader (45.6°) peaks, indicating the presence of polycrystalline Nb_2CT_x and amorphous Ni_xB in the final composite. The broad and diffuse peak observed for Ni_xB at ~45.6° is characteristic of a short-range disordered atomic arrangement with no long-range crystalline order, confirming the amorphous nature of the synthesized Ni_xB (Fig. 1(b)). The absence of any sharp crystalline diffraction peaks further supports this conclusion, consistent with our previously reported data [15,23] and other amorphous Ni_xB materials synthesized via chemical reduction methods [19,21]. There is a broad peak at ~22.37° (Fig. 1(a-e)), which is associated with the microscope glass slide substrate used in the thin film XRD analysis. The position and intensity of the peaks depend on the relative ratio of Ni_xB and Nb_2CT_x in the composite, as well as the chemical interactions between the two materials. Furthermore, the variation in intensity and the shift in peak positions indicate the complete decoration of Ni_xB on the multilayer surface of Nb_2CT_x. The complete decoration of Ni_xB on Nb_2CT_x also increased the interlayer spacing of the MXene layers by diminishing the Al peak, further confirming the successful intercalation of Ni_xB onto MXene. Overall, the XRD results confirm that the effective etching of Al using HF is a feasible approach for producing multilayer Nb_2CT_x, and the introduction of Ni_xB helps prevent the restacking of MXene by enhancing the interlayer spacing. These XRD results are also consistent with the morphological findings (Fig. 2).

The morphological variation of Nb_2CT_x MXene from Nb_2AlC and the decoration of Ni_xB on Nb_2CT_x were further analyzed by FE-SEM. Fig. *S1* depicts the dense, ceramic-like compact structure of the parent Nb_2AlC MAX phase. The exfoliated Nb_2CT_x MXene, obtained through HF etching, exhibits a multi-layered, accordion-like structure, as shown in Fig. 2(a-c). The 2D multilayered structure of Nb_2CT_x MXene confirms the successful etching of Al through the intercalation of F^- ions on the dense surface of Nb_2AlC. Fig. 2(a) shows that the Nb_2CT_x MXene surface is thinner and uniformly stacked in a layer-by-layer architecture, similar to that of Ti-MXenes. The presence of a uniformly stacked layer structure confirms the occurrence of interlayer expansion and enhanced active sites compared to the MAX phase, which is also consistent with the XRD findings. This increased interlayer spacing in Nb_2CT_x MXene facilitates charge transport through rapid intercalation or diffusion, thus enhancing electrochemical energy storage performance. Subsequently, the decoration of Ni_xB particles on the layers of Nb_2CT_x MXene was further confirmed by Fig. 2(d-f). Fig. 2(d) shows that the Ni_xB nanoparticles are uniformly decorated on each layer of Nb_2CT_x. From the high-magnification FE-SEM images (Fig. 2(e,f)), a large number of Ni_xB nanoparticles can be observed on both the surface and edges of the Nb_2CT_x layers, indicating close contact between the two components. The FE-SEM images indicate that the chemically etched Nb_2CT_x MXene layers are synergistically interconnected with Ni_xB particles, which helps to hinder restacking and create a conductive path for improved electrode kinetics during charge/discharge process. Additionally, the FE-SEM mapping image in Fig. 3(a-g) further confirms the presence of elements such as niobium (Nb), carbon (C), oxygen (O), and fluorine (F) in the etched Nb_2CT_x MXene. This also confirms that the Al layer is almost removed, and the MAX phase is successfully etched by HF. Furthermore, the mapping images in Fig. 3(e, f) confirm the presence of nickel (Ni) and boron (B), along with the MXene components, indicating the formation of a 0D/2D composite by a simple in-situ reduction process. Although HR-TEM characterization was not available in the present study, the combined FE-SEM, XRD, XPS, and electrochemical analyses consistently indicate close interfacial contact and synergistic interactions between Ni_xB nanoparticles and Nb_2CT_x nanosheets.

XPS analysis confirmed the successful formation of Nb_2CT_x and Ni_xB/Nb_2CT_x. The survey spectra of Nb_2CT_x revealed the presence of Nb, C, O, F, and Al (Fig. *S2*(a')). In contrast, the XPS survey spectrum of the Ni_xB/Nb_2CT_x composite additionally revealed Ni and B signals (Fig. *S2* (b')), confirming the successful formation of Ni_xB on the Nb_2CT_x sheets. The Nb 3d region was deconvoluted into four components. The low-binding-energy peaks at 203.8 and 206.5 eV correspond to the Nb $3d_{5/2}$ and Nb $3d_{3/2}$ of Nb—C, respectively. Peaks at 206.8 and 209.6 eV are attributed to surface-oxidized Nb_xO_y residues. The calculated spin-orbit splitting values ($\Delta E = 3d_{3/2} - 3d_{5/2}$ are 2.7 and 2.8 eV for Nb—C and Nb—O, respectively (Fig. 4(a)) [26]. The Ni_xB/Nb_2CT_x composite exhibited similar binding-energy positions for Nb—C and Nb—O (Fig. 4 (d)). These results are consistent with those reported by Halim et al. regarding the binding-energy positions and surface niobium oxides [27]. The C 1s region was fitted into four components at 281.9, 284.5, 286.1,

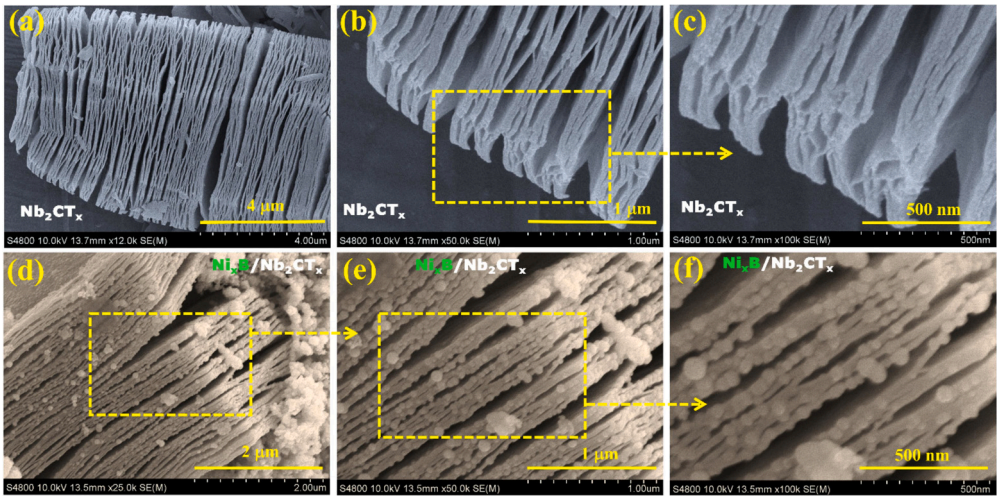

Fig. 2. FE-SEM images of (a-c) Nb_2CT_x MXene, and (d-f) low-high magnification images of Ni_xB/Nb_2CT_x-50 composites.

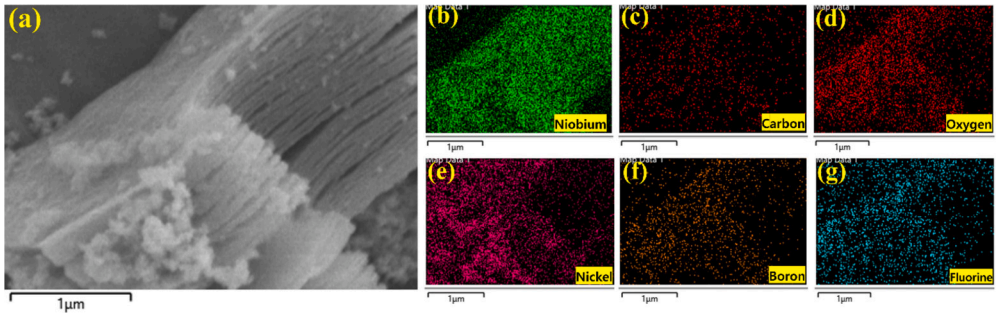

Fig. 3. FE-SEM image and corresponding elemental mapping of the Ni_xB/Nb_2CT_x composite: (a) FE-SEM image, and elemental maps of (b) Nb, (c) C, (d) O, (e) Ni, (f) B, and (g) F.

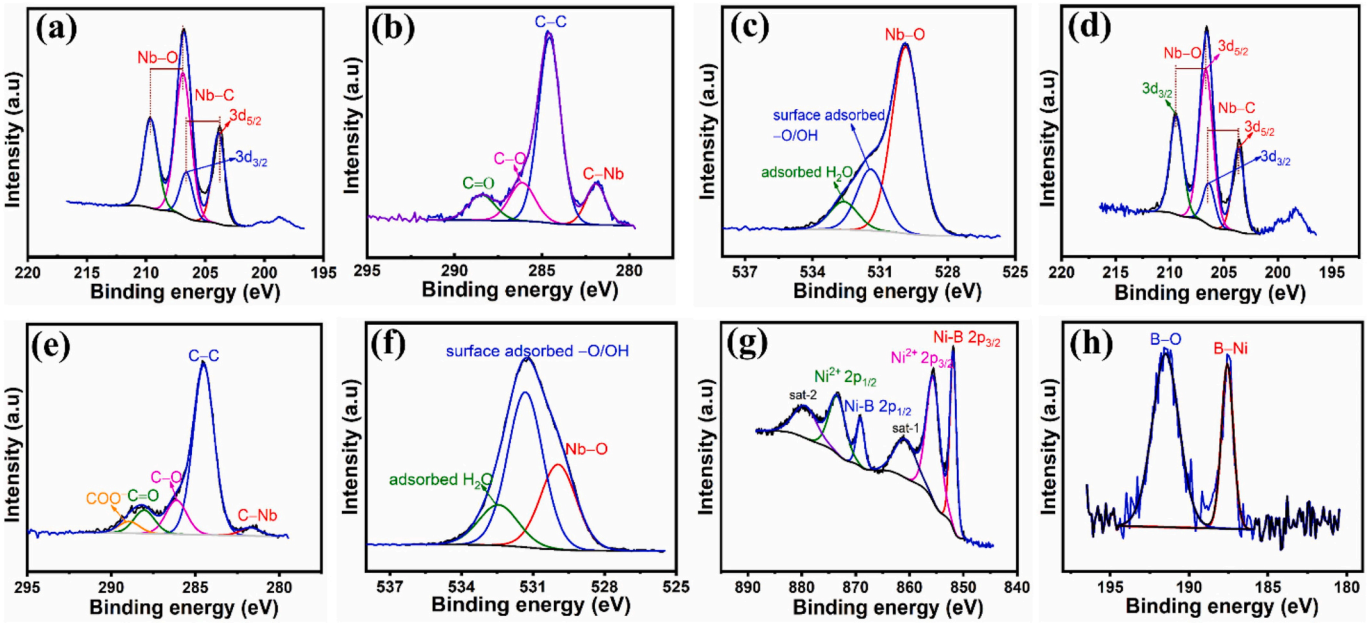

Fig. 4. (a-c) Nb_2CT_x region deconvoluted (a) Nb 3d, (b) C 1s, (c) O 1s and (d-h) Ni_xB/Nb_2CT_x region deconvoluted (d) Nb 3d, (e) C 1s, (f) O 1s, (g) Ni 2p, and (h) B 1s.

and 288.4 eV, corresponding to Nb—C, C—C, C—O, and C═O, respectively (Fig. 4(b)) [28]. The Ni_xB/Nb_2CT_x composite showed similar features, with an additional contribution from carboxylate groups introduced during surface carboxylation in the Ni_xB synthesis process (Fig. 4(e)). The O 1s spectra of both samples were deconvoluted into three components assigned to Nb—O, surface-bound O/OH groups, and adsorbed H_2O (Fig. 4 (c), (f)). Al 2p peaks were observed at 75.5 eV ($2p_{3/2}$) and 75.9 eV ($2p_{1/2}$), originating from aluminum oxides formed during the MAX-phase etching process (Fig. *S2*(b,c)). The detected Al 2p peak, corresponding to Al_2O_3, is observed with relatively low intensity compared to the dominant Nb 3d and C 1s signals, indicating only trace amounts of residual aluminum remaining after HF etching. Such residues are commonly observed in etching-derived MXene systems and are generally electrochemically inactive in alkaline electrolyte, as Al_2O_3 is a stable oxide that does not undergo significant redox reactions within the operating potential window. Therefore, the contribution of residual Al species to the overall charge storage mechanism is considered negligible. The F 1s peak at 685.7 eV corresponds to Nb–O–F species, with almost similar positions observed for both pristine Nb_2CT_x and Ni_xB/Nb_2CT_x (Fig. *S2*(d,e)), indicating the presence of surface —F terminations originating from the HF etching process. These —F groups are commonly observed in MXenes and are generally considered electrochemically less active. The high intensity of the F 1s peak suggests a significant concentration of —F terminal groups on the MXene surface, which can partially reduce surface conductivity and limit ion-accessible active sites. However, the —F terminations do not block ion intercalation channels between the MXene layers, as evidenced by the *b*-value analysis confirming a mixed diffusion-controlled and capacitive charge storage mechanism. Furthermore, the incorporation of amorphous Ni_xB provides additional electrochemically active interfaces that compensate for the reduced accessibility caused by —F terminations, facilitating fast charge transfer and electrolyte ion adsorption through interfacial redox reactions. In the composite, the Ni 2p region showed two spin-orbit doublets. The low-binding-energy peaks at 851.9 eV ($2p_{3/2}$) and 869.1 eV ($2p_{1/2}$) correspond to metallic Ni bonded with boron (Ni—B), while the higher-binding-energy peaks at 855.5 eV ($2p_{3/2}$) and 873.4 eV ($2p_{1/2}$) are attributed to Ni^{2+} species (Fig. 4(g)). The calculated ΔE values of 17.2 and 17.9 eV match those expected for Ni—B and Ni^{2+}, respectively [29]. The B 1s spectrum exhibits two peaks at 187.6 and 191.4 eV, assigned to Ni—B and boron oxide (B—O), respectively (Fig. 4 (h)). The presence of B—O is due to the rapid surface oxidation of metal borides upon air exposure, consistent with the observations of *Gouget* et al. [30]. Notably, the B binding energy in Ni_xB (187.6 eV) is shifted by +0.5 eV relative to elemental boron (187.1 eV), suggesting partial electron donation from boron to nickel. Overall, the formation of a Ni_xB/Nb_2CT_x composite is expected to enhance electrical conductivity and provide active Ni redox sites, offering promise for high-performance supercapacitor applications. The detailed elemental assignment,

binding energy, FWHM, and area values are presented in Table S1.

The electrochemical behavior of Nb_2CT_x MXene, Ni_xB and Ni_xB/Nb_2CT_x composites was evaluated using CV, GCD, and EIS measurements. The experiments were designed to evaluate the charge storage capability of the Nb_2CT_x electrode and to investigate the influence of varying Nb_2CT_x content on the electrochemical performance and stability of the Ni_xB/Nb_2CT_x composite. Carbon cloth (CC) was used as the conductive substrate for all electrode preparations. The electrochemical contribution of bare CC was confirmed to be negligible, as the CV recorded at 10 mV s^{-1} shows a maximum current density of approximately 0.001 A g^{-1}, which is orders of magnitude lower than that of the composite electrodes (Fig. *S3*). Fig. 5(a) represents the CV curves for Nb_2CT_x/CC, Ni_xB/CC, Ni_xB/Nb_2CT_x-25/CC, Ni_xB/Nb_2CT_x-50/CC, and Ni_xB/Nb_2CT_x-150/CC electrodes. The CV experiment was performed at an applied scan rate of 10 mV s^{-1} in an electrolyte medium of 3 M KOH, with an operating voltage window of 0 to 0.55 V. The CV curve for pure Nb_2CT_x MXene in Fig. 5(a) shows the absence of distinct redox peaks but exhibits a broad anodic and cathodic counterpart, indicating the electric double layer behavior of Nb_2CT_x MXene, which originates from the intercalation/de-intercalation process. The integral area for Nb_2CT_x MXene is lower compared to the other Ni_xB and Ni_xB/Nb_2CT_x electrodes. This could be attributable to the larger interlayer spacing of the Ni_xB modified Nb_2CT_x, which allows faster adsorption and intercalation of ions, thereby enhancing charge transport and improving electrochemical behavior. The Ni_xB/CC electrode showed a well-defined quasi-reversible peak, and its integral area is higher than that of Nb_2CT_x MXene, indicating that the charge storage is mainly due to the redox reaction. This originates from their smaller particle size and amorphous phase of Ni_xB, which provides more active sites for better accessibility of ions during the redox reaction. Based on the activity of both pristine Nb_2CT_x and Ni_xB, different ratios of Ni_xB/Nb_2CT_x-25/CC, Ni_xB/Nb_2CT_x-50/CC, and Ni_xB/Nb_2CT_x-150/CC electrodes were tested. From the CV curves, it is clearly seen that all electrodes show similar quasi-reversible redox behavior with a slight shift in peak positions, indicating characteristics typical of battery-type materials. Additionally, the integral area of all electrodes is higher than that of Nb_2CT_x/CC and Ni_xB/CC, indicating a significant influence on charge-storage capacitance due to the variation in Nb_2CT_x content in Ni_xB/Nb_2CT_x. This could be related to the increased Nb_2CT_x layers, which provide more active sites for the integration of Ni_xB on the surface and edges. However, the electrochemical performance of Ni_xB/Nb_2CT_x-150/CC is lower than that of Ni_xB/Nb_2CT_x-25/CC and Ni_xB/Nb_2CT_x-50/CC, indicating the occurrence of re-stacking phenomena due to the increase in Nb_2CT_x, which blocks the active sites in the layers and reduces electrochemical performance toward charge storage. Similar to Ni_xB/Nb_2CT_x-150/CC, the Ni_xB/Nb_2CT_x-25/CC shows a lower integral area and less capacitive behavior than Ni_xB/Nb_2CT_x-50/CC, indicating less decoration of Ni_xB on the multilayers of Nb_2CT_x. These CV results conclude that the optimum condition for enhancing the electrochemical performance of Ni_xB/Nb_2CT_x is achieved with the introduction of Nb_2CT_x-50. The charge storage mechanism of the Ni_xB/Nb_2CT_x is attributed to reversible redox transitions of Nb and Ni species in alkaline electrolyte, consistent with previously reported —F terminated MXene and Ni-based pseudocapacitive systems [13,15,17]. Overall, the superior capacitive storage behavior of Ni_xB/Nb_2CT_x-50/CC originates from its well-integrated composite structure, abundant accessible active sites, and enlarged specific surface area, which synergistically facilitate the redox process and enhance charge storage performance.

To further investigate the enhanced charge storage behavior of Ni_xB/Nb_2CT_x, CV analysis was performed with different scan rates, ranging from 3, 5, 7, 10, 15, 20, 30, and 50 mV s^{-1}, under the same operating conditions. The corresponding CV curves for Ni_xB/CC, Ni_xB/Nb_2CT_x-25/CC, and Ni_xB/Nb_2CT_x-150/CC are shown in Fig. *S4*. It can be clearly seen that the peak current increases with the scan rate for Ni_xB/CC, representing a quasi-reversible nature due to the involvement of the faradaic process. Similarly, the Ni_xB/Nb_2CT_x-25/CC and Ni_xB/Nb_2CT_x-150/CC

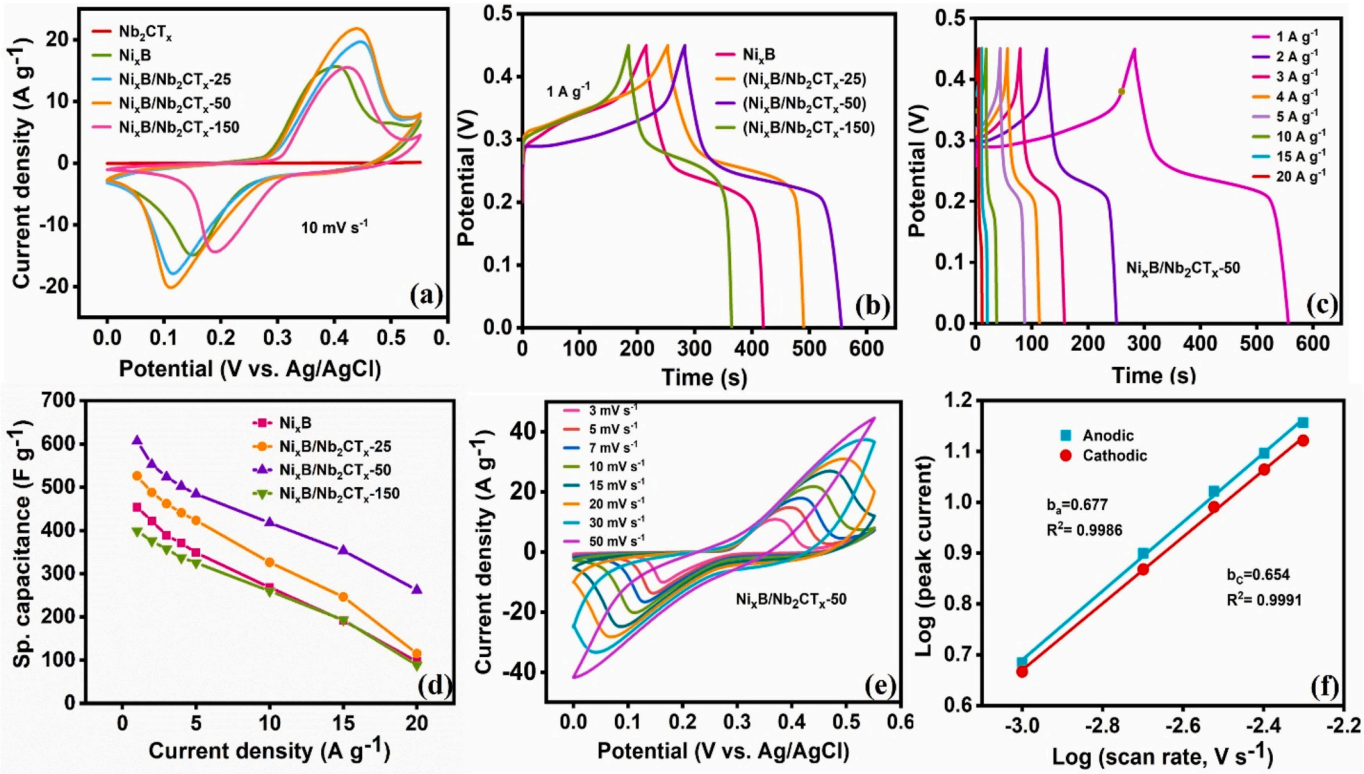

Fig. 5. (a) CV curves for all electrodes plotted at a scan rate of 10 mV s^{-1} (b) GCD curves for all electrodes recorded at a current density of 1 A g^{-1}, (c) GCD curves for the Ni_xB/Nb_2CT_x-50 electrode recorded at different current densities (1–20 A g^{-1}), (d) Current density vs. Specific capacitance, (e) CV curves for the Ni_xB/Nb_2CT_x-50 electrode at different scan rates (3–50 mV s^{-1}), (f) Corresponding linear plot of logarithm of peak current vs. logarithm of scan rate.

electrodes also exhibit a pair of quasi-reversible peaks in the CV curves, indicating low charge transfer resistance and fast faradaic response at the electrode/electrolyte interface. These CV results also confirm that the introduction of Ni_xB onto the Nb_2CT_x layers significantly enhances the electrochemical storage process. This improvement is due to the easy accessibility of ions through the particulate architecture of Ni_xB, which effectively inhibits the restacking of Nb_2CT_x and promotes the rapid intercalation and deintercalation of ions during the charge storage process. Based on this, the electrochemical energy storage capability of Nb_2CT_x after the introduction of Ni_xB was estimated by GCD analysis. The GCD test was performed for Ni_xB/CC, Ni_xB/Nb_2CT_x-25/CC, Ni_xB/Nb_2CT_x-50/CC, and Ni_xB/Nb_2CT_x-150/CC by applying various current densities (1, 2, 3, 4, 5, 10, 15, and 20 A g^{-1}) under an operating potential window of 0 to 0.45 V. The GCD potential window was intentionally narrowed to 0–0.45 V compared to the CV window of 0–0.55 V to avoid interference from the onset of water oxidation observed at higher potentials and to ensure stable and reproducible charge-discharge behavior. Fig. 5(b, c) and Fig. *S5* show that all the electrodes exhibit almost linear and symmetrical rectangular charge-discharge curves, indicating the occurrence of a reversible redox process at the electrode-electrolyte interface. The specific capacitance of Ni_xB/Nb_2CT_x-25/CC, Ni_xB/Nb_2CT_x-50/CC, and Ni_xB/Nb_2CT_x-150/CC at 1 A g^{-1} were determined to be 526.0 F g^{-1}, 606.7 F g^{-1}, and 399 F g^{-1}, respectively. Similar to the Ni_xB/Nb_2CTx electrodes, the Ni_xB/CC exhibited a similar symmetrical curve and had a specific capacitance value of 453.4 F g^{-1} at 1 A g^{-1}. When the current density reached 20 A g^{-1}, all electrodes showed a lower specific capacitance compared to the lower current densities. At 20 A g^{-1}, Ni_xB/CC exhibited a specific capacitance of 97.1 F g^{-1}, which is lower than other electrodes, such as Ni_xB/Nb_2CT_x-25/CC (115.54 F g^{-1}), Ni_xB/Nb_2CT_x-50/CC (262.2 F g^{-1}), and Ni_xB/Nb_2CT_x-150/CC (88.88 F g^{-1}). The corresponding plots of current density versus specific capacitance for all electrodes are presented in Fig. 5(d). The plots show a decrease in specific capacitance with an increase in current density, indicating the inability of the electrodes to participate in the redox reaction due to the blocking of active sites, which hinders the migration of ions through the electrolyte. Specifically, the electrochemical capacitive performance of the Ni_xB electrode decreased when the Nb_2CT_x amount increased from 25 to 150 mg. This reduction in capacitance is likely the result of the excessive amount of Nb_2CT_x in the composite, which may block the active sites due to restacking or aggregation phenomena, thereby hindering overall electrochemical performance. In contrast, the Ni_xB/Nb_2CT_x-50/CC shows higher specific capacitance than the other electrodes, mainly due to its wider interlayer spacing, which provides abundant active sites with an increased surface area compared to pristine Nb_2CT_x. This structure can accommodate a larger number of ions during the charge/discharge process without exhibiting structural deformity. Particularly, the improved capacitive behavior of the optimized Ni_xB/Nb_2CT_x-50/CC suggests that the intercalation and adsorption of Ni_xB on each Nb_2CT_x layer induces a conduction path by creating more transport channels for the rapid diffusion/migration of ions, thereby facilitating the redox process during charge storage.

To understand the energy storage mechanism of Ni_xB/Nb_2CT_x-50/CC, the CV analysis was performed at different scan rates (3, 5, 7, 10, 15, 20, 30, and 50 mV s^{-1}) within the same potential window. The CV curves in Fig. 5(e) show that the peak current increases with an increase in scan rates from lower to higher. As the scan rate increases, both the anodic and cathodic peaks shift in the positive and negative directions, respectively. This shift is attributed to the polarization of electrode material, which increases the intrinsic resistance and slows the charge transfer kinetics during the charge-discharge process. Although redox peaks are observed at all scan rates, indicating good reversibility of the electrode, these peaks are likely related to the intercalation/de-intercalation process. Further, the variation in anodic and cathodic peak currents and the electrode's kinetic mechanism were explored using the power law eqs. (1) and (2).

$$i = a\nu^b \tag{1}$$

$$\log i = b \log \nu + \log a \tag{2}$$

where the parameters a and b are variables. It is well known that the total observed peak current is the sum of diffusion and surface-controlled processes. From the linear plot between log i and log ν (Fig. 5(f)), the slope value is obtained as $b = 0.677$ for the anodic peak and $b = 0.654$ for the cathodic peak of Ni_xB/Nb_2CT_x-50/CC. The obtained b-values indicate that the charge-storage kinetics are governed by a combination of surface-controlled (capacitive) and diffusion-controlled processes, suggesting that both surface redox reactions and ion intercalation contribute to the overall electrochemical behavior. These results indicate a mixed charge-storage mechanism rather than a purely capacitive or diffusion-controlled process. To clarify the charge storage mechanism of the Ni_xB/Nb_2CT_x-50/CC, Dunn's method was applied using eq. (3),

$$I = k_1\nu + k_2\nu^{1/2} \tag{3}$$

Based on previous studies [23], the constant terms k_1 and k_2 values were determined. The obtained values were substituted into eq. (3) to calculate the percentage contribution of the electrode charge-transfer kinetics. The CV curves for the percentage contribution (Fig. 6(a-e)) and their bar plot are shown in Fig. 6(f), which reveals that the storage mechanism of the Ni_xB/Nb_2CT_x-50/CC consists of 87.4% capacitive contribution and 12.6% diffusion-controlled process at a scan rate of 1 mV s^{-1}. At 5 mV s^{-1}, the capacitive contribution increases to 93.9%, indicating that rapid electron transport at higher scan rates limits the contribution of the diffusion-controlled process. The proportion of charge storage for Ni_xB/Nb_2CT_x-50/CC shows a slight contribution from the diffusion-controlled charge storage mechanism at low scan rates, but the capacitive-controlled charge storage mechanism increases consistently from lower to higher scan rates. These results are consistent with the power-law analysis, which indicates that both capacitive and diffusion-controlled processes contribute to charge storage. Dunn's analysis further quantifies the relative contribution of each process at different scan rates.

Overall, the CV and GCD results show that the Ni_xB/Nb_2CT_x electrode exhibits significantly improved charge storage properties compared to the pristine materials. In general, the electrochemical performance of the Ni_xB/Nb_2CT_x composite mainly originates from its multidimensional structure, which combines the properties of the individual materials. The multilayer architecture of Nb_2CT_x exhibits good intrinsic activity and enhances electrical conductivity. Furthermore, the combination with Ni_xB increases the interlayer spacing, prevents restacking, and thereby improves charge transport, facilitating the rapid intercalation and de-intercalation of ions during the cyclic charging process. More importantly, the 0D/2D composite architecture preserves the beneficial structural features of both components, resulting in enhanced energy storage and improved cycling stability through synergistic interactions.

The Nyquist plots of Ni_xB/CC, Ni_xB/Nb_2CT_x-25/CC, Ni_xB/Nb_2CT_x-50/CC, and Ni_xB/Nb_2CT_x-150/CC composite electrodes obtained from EIS are shown in Fig. *S6*(a), with magnified individual panels provided in Fig. *S6*(c-f) for clear discrimination against impedance values. To extract quantitative resistance values, the experimental data were fitted using the Randles equivalent circuit model: $R_s(Q_1(R_{ct}W)Q_2)$ (Fig. *S6*). In the Nyquist plot, the intercept of the high-frequency arc region on the real axis corresponds to the series resistance (R_s) [31]. The R_s values for the Ni_xB/CC, Ni_xB/Nb_2CT_x-25/CC, Ni_xB/Nb_2CT_x-50/CC, and Ni_xB/Nb_2CT_x-150/CC electrodes were determined to be 0.99, 2.68, 2.00, and 2.08 Ω, respectively. The diameter of the semicircle in the medium-frequency region is associated with the charge transfer resistance (R_{ct}). The inverse of R_{ct} is related to the rate of charge transfer processes, following the relationship: $\frac{1}{R_{ct}} \propto e^{-Eb/KT}$ where E_b is the activation energy, k

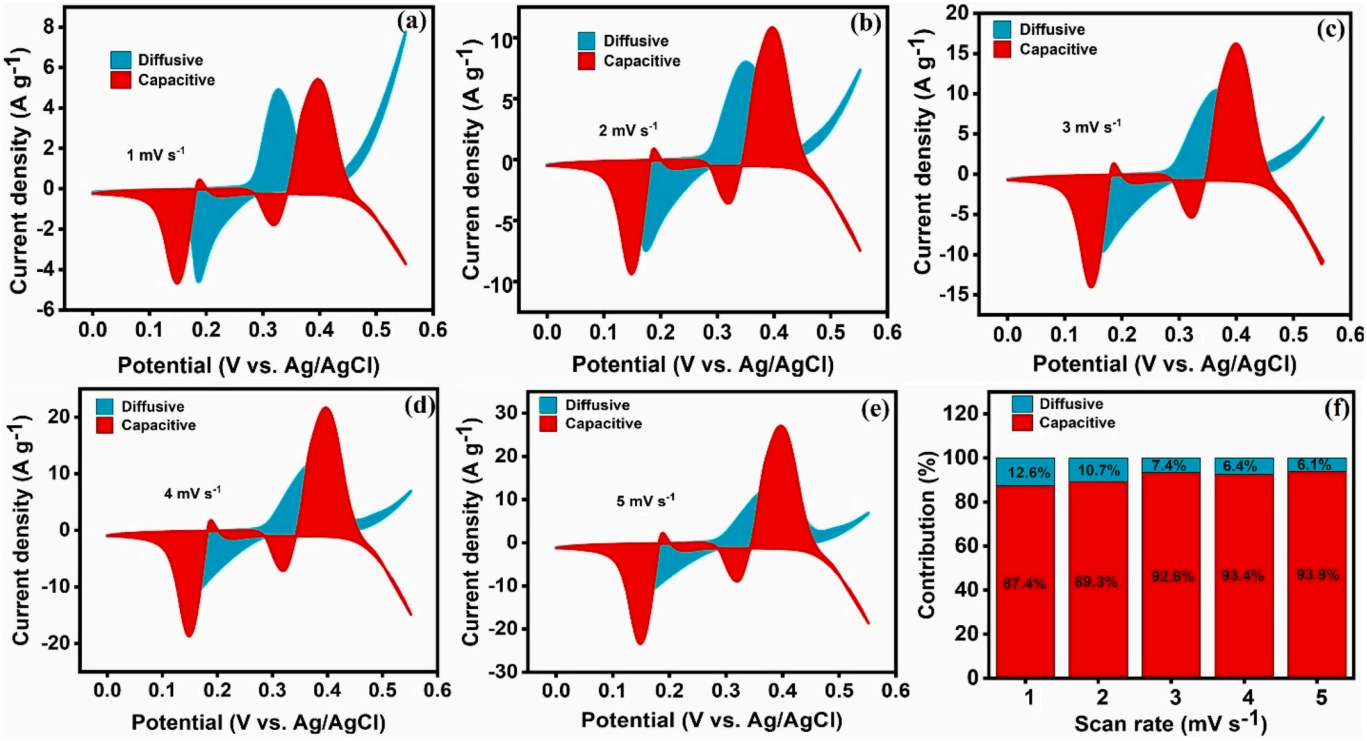

Fig. 6. (a-e) Shaded CV curves for diffusive and capacitive contributions recorded at 1 to 5 mV s^{-1} and (f) percentage contribution of diffusive and capacitive contributions as a function of scan rates.

is the Boltzmann constant, and *T* is the temperature [32,33]. Among the tested electrodes, Ni_xB/CC and Ni_xB/Nb_2CT_x-50/CC exhibited lower R_{ct} values of 1.17 Ω and 2.18 Ω, respectively, compared to Ni_xB/Nb_2CT_x-25/CC and Ni_xB/Nb_2CT_x-150/CC. This suggests that the Ni_xB/Nb_2CT_x-50/CC composite possesses relatively lower activation energy for charge transfer. Although the R_{ct} of Ni_xB/CC is slightly lower than that of Ni_xB/Nb_2CT_x-50/CC, the Warburg (diffusion) resistance is lower in the latter, indicating improved ion diffusion. From the EIS result, it is evident that the variation in R_{ct} is not determined solely by the amount of MXene, but rather by the overall microstructure, dispersion of Ni_xB and interfacial contact between Ni_xB and Nb_2CT_x. At the optimal loading (Ni_xB/Nb_2CT_x-50), close interfacial contact between Ni_xB and Nb_2CT_x facilitates efficient electron transport, resulting in the lowest R_{ct} (2.18 Ω). In contrast, at lower loading (25%), insufficient coverage of Ni_xB leads to less effective interfacial contact and higher resistance (17.71 Ω). When the MXene content is further increased to 150%, excessive Nb_2CT_x leads to restacking and aggregation of MXene layers, which blocks ion diffusion pathways and reduces effective contact between electroactive components. This structural restacking increases both ionic and charge transfer resistance, resulting in a higher R_{ct} value. Therefore, the observed trend is not anomalous but rather reflects the balance between interfacial formation and MXene restacking effects. Overall, the electrochemical impedance is strongly dependent on morphology and interfacial engineering rather than composition alone.

The fitted EIS parameters for all electrodes are summarized in Table *S2*. Furthermore, the enhanced electronic transport characteristics during the charge-discharge process for the Ni_xB/Nb_2CT_x-50/CC electrode are supported by its low diffusion resistance (σ), as shown in the Z' vs. ω plot (Fig. *S6*(b)). The diffusion resistance σ was calculated using Eq. (4) [34].

$$Z_w = \sigma\omega^{-1/2} - j\sigma\omega^{-1/2} \tag{4}$$

Where $\sigma\omega^{-1/2}$ is the real impedance (Z'), $j\sigma\omega^{-1/2}$ is the imaginary impedance (Z") and Z_w represents the Warburg or diffusion resistance. The σ value was determined from the slope of the linear fit of the plot in Fig. S6(a). The calculated σ values are 119.26 Ω $s^{-1/2}$ (Ni_xB/CC), 33.72 Ω $s^{-1/2}$ (Ni_xB/Nb_2CT_x-25/CC), 10.73 Ω $s^{-1/2}$ (Ni_xB/Nb_2CT_x-50/CC), and 167.30 Ω $s^{-1/2}$ (Ni_xB/Nb_2CT_x-150/CC). The Ni_xB/Nb_2CT_x 50/CC electrode shows the lowest diffusion resistance among all samples. The hydroxyl ion diffusion coefficient (D_{OH}-) was further calculated based on eq. (5) [33].

$$D_{OH^-} = \frac{1}{2}\left(\frac{RT}{AF^2n^2C\sigma_w}\right)2 \tag{5}$$

where *R* is the gas constant (J mol^{-1} K^{-1}), *T* is the temperature (K), *A* is the electrode area (cm^2), *F* is the Faraday constant (C mol^{-1}), *n* is the number of electrons transferred (assumed to be 1 for the nickel boride redox couple), σ_w is the warburg coefficient, and *C* is the molar concentration of hydroxyl ions (mol cm^{-3}). The calculated D_{OH}- values are as follows: 2.77×10^{-13} cm^2 s^{-1} (Ni_xB/CC), 3.46×10^{-12} cm^2 s^{-1} (Ni_xB/Nb_2CT_x-25/CC), 3.42×10^{-11} cm^2 s^{-1} (Ni_xB/Nb_2CT_x-50/CC), and 1.41×10^{-13} cm^2 s^{-1} (Ni_xB/Nb_2CT_x-150/CC). The significantly higher D_{OH}- value for Ni_xB/Nb_2CT_x-50/CC suggests that it effectively utilizes the MXene layers to facilitate ion accessibility within the 2D layered structure. In conclusion, the impedance and diffusion analyses (σ and D_{OH}-) align well with the CV and charge-discharge performance results, further confirming the superior electrochemical properties of the Ni_xB/Nb_2CT_x-50/CC electrode. Fig. S7 presents the Bode impedance plots of all electrodes (Ni_xB/CC, Ni_xB/Nb_2CT_x-25/CC, Ni_xB/Nb_2CT_x-50/CC, and Ni_xB/Nb_2CT_x-150/CC). As shown in Fig. S7(a), the impedance amplitude of most modified electrodes is nearly independent in the high-frequency region; however, it becomes frequency-dependent below 2.5 Hz. Among all samples, Ni_xB/Nb_2CT_x-50/CC exhibits the lowest impedance. The phase profile of pristine Ni_xB shows a single peak at 3.4 Hz, whereas the MXene-containing electrodes display two distinct phase peaks (Fig. S7(b)). In particular, Ni_xB/Nb_2CT_x-50/CC exhibits peaks at 0.73 and 3.5 Hz. These results are consistent with the lowest diffusion resistance and the highest OH^- diffusion coefficient obtained from the calculations.

The long-term cycling stabilities of Ni_xB/Nb_2CT_x-50/CC and Ni_xB/CC electrodes were evaluated over 10,000 charge-discharge cycles in a three-electrode configuration (Fig. *S8*(a)). The composite electrode retains 60.8% of its initial capacitance after 10,000 cycles, demonstrating significantly improved durability compared to pure Ni_xB, which retains only 13.5% under the same conditions. The rapid capacity fading of pure Ni_xB is attributed to nanoparticle agglomeration during prolonged cycling, which progressively reduces the accessible electroactive surface area. For the composite, the moderate capacity fading is mainly associated with the presence of —F surface terminations on Nb_2CT_x, which partially block electroactive sites and hinder ion transport, along with gradual surface oxidation of the MXene layers during extended cycling in alkaline electrolyte. Nevertheless, post-cycling SEM analysis confirms that the Ni_xB/Nb_2CT_x-50 composite largely retains its morphology and interfacial connectivity after 10,000 cycles (Fig. S9), indicating that the composite architecture effectively suppresses Ni_xB agglomeration and mitigates structural degradation. The retained layered structure and distributed Ni_xB nanoparticles after prolonged cycling in 3 M KOH suggest that no severe oxidative structural collapse of the Nb_2CT_x phase occurred, which is further supported by the consistently high Coulombic efficiency of 95.4% maintained throughout 10,000 cycles. These results demonstrate that the composite maintains reasonable cyclic stability even under demanding conditions where MXene surface oxidation and substrate degradation are anticipated. The observed stability is consistent with previously reported studies on MXene-based composite electrodes [35–38].

4. Performance of the Ni_xB/Nb_2CT_x-50//rGO device

To further evaluate the performance of the optimized Ni_xB/Nb_2CT_x-50 electrode, an asymmetric supercapacitor (ASC) device was assembled by coupling Ni_xB/Nb_2CT_x-50 as the positive electrode with reduced graphene oxide (rGO) as the negative electrode (Ni_xB/Nb_2CT_x-50//rGO). The mass loading of each electrode was determined using the charge balance equation (Eq. S1). Based on this calculation, the mass ratio of Ni_xB/Nb_2CT_x-50 to rGO was set at 1:1.56 (1.3 mg: 2.02 mg), giving a total active mass of 3.32 mg. The CVs recorded for the Ni_xB/Nb_2CT_x-50//rGO device at various scan rates from 5 to 100 mV s^{-1} are shown in Fig. 7(a). Broad oxidation and reduction waves are seen, and these can be attributed to the inter-conversions between the Nb oxidation states in the MXene phase and the Ni oxidation states in the Ni_xB [15,17]. These waves shift to less favorable oxidation and reduction potentials on increasing the scan rate, and this is consistent with the surface-confined redox reactions of the Nb and Ni. The CVs depicted in Fig. 7(b) show that the Ni_xB/Nb_2CT_x-50//rGO can be cycled to a relatively high potential of 1.65 V without any loss in activity or alteration to the general shape of the CVs, indicating very good stability. The corresponding GCD curves are presented in Fig. 7(c), while similar data recorded at different current densities are provided in Fig. 7(d). Excellent stability is evident with very good symmetry in the GCD curves. This suggests very similar charging and discharging periods with higher upper potentials of 0.9, 1.1, 1.3, 1.5, and 1.65 V. However, at an upper potential of 1.7 V, instability is seen, and this appears to be connected to the onset of the oxygen evolution reaction (OER). Likewise, excellent reversibility is evident at current densities ranging from 1 to 20 A g^{-1}. In Fig. 7(e), specific capacitance is presented as a function of the current density and shows a clear decrease with increasing current density values. For example, at a current density of 1 A g^{-1}, the specific capacitance is 123.6 F g^{-1} (204.1C g^{-1}), but decays to 2.4 F g^{-1} (4C g^{-1}) at the higher current density of 20 A g^{-1}.

The long-term cyclic stability of the assembled Ni_xB/Nb_2CT_x/CC//rGO/CC ASC was further evaluated over 10,000 charge-discharge cycles (Fig. S8(b)). The device exhibits a rapid capacity fading within the first 200 cycles, dropping to 15.3% of its initial capacitance, after which the device enters a relatively stable regime with a final capacity retention of 8.07% at 10,000 cycles. It should be noted that the capacity fading observed in the full asymmetric device is not solely reflective of the active material's intrinsic electrochemical stability, as confirmed by the three-electrode measurements, but rather a combined result of mechanical degradation of both CC substrates, increased interfacial

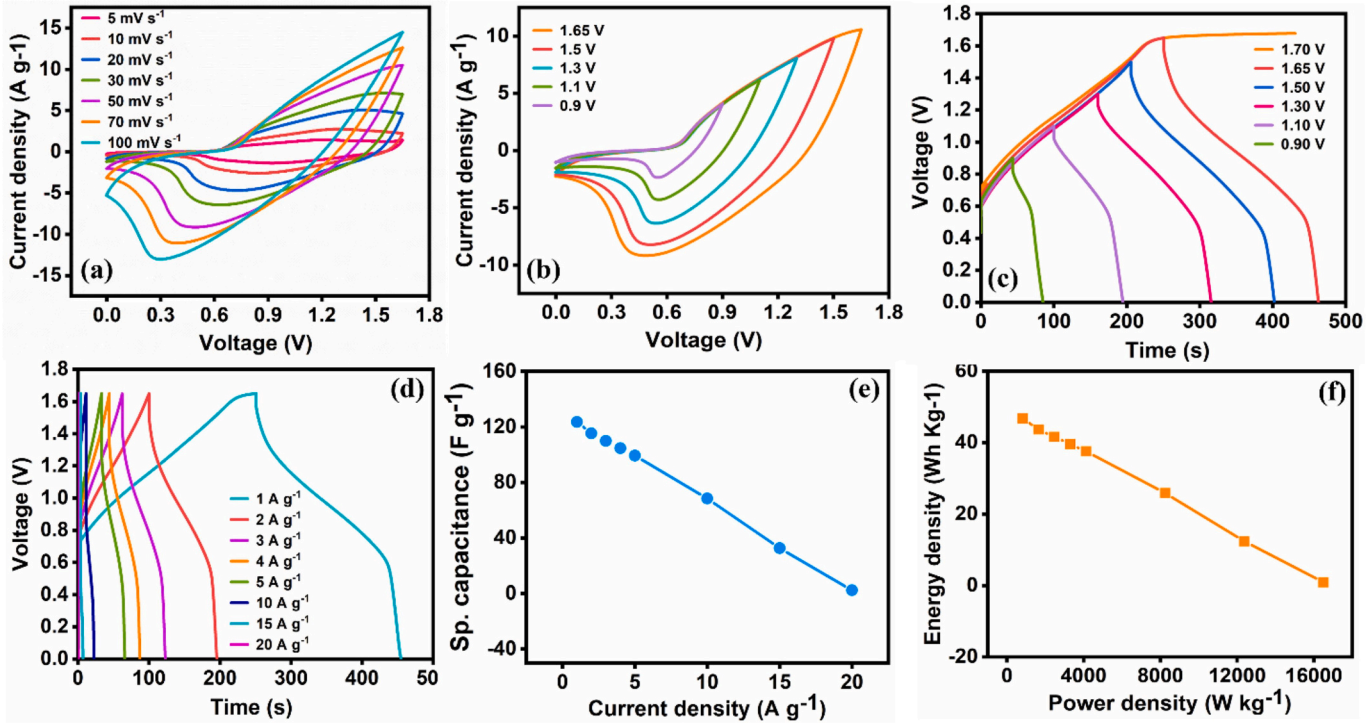

Fig. 7. (a) CVs recorded at scan rates from 5 to 100 mV s^{-1} between 0 and 1.65 V, (b) CV at different potentials from 0.90 to 1.65 V, GCD curves recorded at (c) various upper potentials ranging from 0.90 to 1.70 V, (d) GCD at different current densities for the Ni_xB/Nb_2CT_x-50//rGO device, (e) Current density vs. Specific capacitance. (f) Energy density as a function of power density for Ni_xB/Nb_2CT_x//rGO.

resistance at the separator, and the cumulative stress of operating two electrodes simultaneously under prolonged alkaline conditions. The fiber loosening and progressive delamination of the active material from the CC current collector under repeated ion insertion and extraction further contribute to the observed fading. Importantly, despite the capacity fading, the device maintains a consistently high Coulombic efficiency of 95.4% throughout the entire 10,000 cycles, confirming that the faradaic charge transfer process remains highly reversible and that the capacity loss originates from mechanical and interfacial degradation of the CC rather than irreversible electrochemical side reactions. The impedance data recorded for the Ni_xB/Nb_2CT_x//rGO device are shown in a Nyquist plot in Fig. S10. A semicircle is evident at the higher frequencies, while a diffusion tail becomes dominant at lower frequencies, reflecting the formation of a double-layer and ion diffusion kinetics at the lower frequencies. The charge-transfer resistance was deduced as 1.22 Ω. Overall, the plot indicates favorable electrochemical kinetics and strong capacitive behavior for the Ni_xB/Nb_2CT_x//rGO. The relationship between energy and power densities is summarized in Fig. 7(f), in the form of a Ragone plot. A high energy density (ED), reaching a value of 46.7 Wh kg^{-1}, is seen at a power density (PD) of 825 W kg^{-1}. However, the ED is reduced as the PD is increased, with an ED of 0.91 Wh kg^{-1} at a PD of 16,500 W kg^{-1}. The obtained electrochemical performance is comparable to recently reported Nb-based MXenes and metal borides-based supercapacitors, including Ta-Nb_2CT_x//AC (ED 47.5 Wh kg^{-1} at 500 W kg^{-1}) [39], Ce-Nb_2CT_x (ED 45 Wh kg^{-1} at 275 W kg^{-1}) [40], $Ti_2NbC_2T_x$ (ED 34.0 Wh kg^{-1} at 331.1 W kg^{-1}) [41], $DyMn_2O_5/Dy_2O_3$/MXene (ED 46.25 Wh kg^{-1} at 705 W kg^{-1}) [42], $Ti_3C_2T_x$/Ni-MOF (ED 19.4 Wh kg^{-1} at 331.8 W kg^{-1}) [43], $YSe_2/MoSe_2/Ni_xB$//AC (ED 39.5 Wh kg^{-1} at 800 W kg^{-1}) [15], $NiCo_2O_4$@Nb_2CTx//AC (ED 45.4 Wh kg^{-1} at 163 W kg^{-1}) [25], and V-(Ni,Co)Se_2@Nb_2CT_x//AC (ED 45.6 Wh kg^{-1} at 168.4 W kg^{-1}) [44], respectively.

5. Conclusion

In this work, a Ni_xB/Nb_2CT_x composite was fabricated using a combination of HF-assisted etching and in-situ chemical reduction. The resulting 0D/2D architecture promotes effective interfacial contact between Ni_xB and Nb_2CT_x, which facilitates electron transport, supports ion diffusion, and improves redox activity. As a result of these combined effects, the optimized Ni_xB/Nb_2CT_x-50 electrode exhibits a high specific capacitance of 606.7 F g^{-1} at 1 A g^{-1}, demonstrating moderate rate capability with a capacitance retention of 43.2% from 1 to 20 A g^{-1}. When assembled into an ASC device as Ni_xB/Nb_2CT_x//rGO, the device delivered a high energy density of 46.7 Wh kg^{-1} at a power density of 825 W kg^{-1}, demonstrating its potential for high-performance energy storage. The electrode was supported by CC, which served as a flexible, conductive, and good current collector, ensuring efficient charge transport and mechanical integrity without contributing to electrochemical activity. However, prolonged stability testing may lead to degradation of the CC substrate, which can affect electrode durability and performance. Overall, this study highlights the crucial role of interfacial and structural engineering in designing amorphous transition metal boride-MXene hybrids for next-generation high energy density supercapacitors.

CRediT authorship contribution statement

Ramaraj Sukanya: Writing – review & editing, Writing – original draft, Visualization, Validation, Methodology, Investigation, Funding acquisition, Formal analysis, Data curation, Conceptualization. **Raj Karthik:** Writing – original draft, Visualization, Investigation, Formal analysis, Data curation, Conceptualization, Methodology. **Chelladurai Karuppiah:** Writing – review & editing, Formal analysis, Data curation, Funding acquisition. **Deivasigamani Ranjith Kumar:** Writing – review & editing, Formal analysis, Data curation. **Milton Ahamed:** Formal analysis, Data curation, Investigation, Visualization, Writing – review & editing. **Hye Jin Lee:** Writing – review & editing. **Carmel B. Breslin:** Writing – review & editing, Writing – original draft, Supervision, Resources, Project administration, Funding acquisition. **Jae-Jin Shim:** Supervision, Resources, Project administration, Funding acquisition, Writing – review & editing.

Declaration of competing interest

The authors declare that they have no known competing financial interests or personal relationships that could have appeared to influence the work reported in this paper.

Acknowledgments

This publication has emanated from research conducted with the financial support of the European Union's Horizon 2020 research and innovation programme under the Marie Skłodowska-Curie grant agreement No 101106064. This work was supported by the National Research Foundation (NRF) of Korea under the Core Research Grants (Type B) Program, funded by the Ministry of Science and ICT (RS-2026-25480159). It was also partially supported by the Regional Innovation System and Education (RISE) Glocal University 30 project through the Daegu RISE Center, funded by the Ministry of Education and the Daegu City (2025-RISE-03-001 to C. Karuppiah).

Appendix A. Supplementary data

Supplementary data to this article can be found online at https://doi.org/10.1016/j.est.2026.123987.

Data availability

Data will be made available on request.

References

[1] W. Yang, Z. Yang, J. Wang, W. Lu, W. Wang, A Bean Catching Double Pigeons: Sonication-Assisted Modification of Nb_2C MXenes Composites by O-Doping Porous Biomass-Carbons for Supercapacitors and Zinc-Ion Batteries, J. Energy Storage 65 (2023) 107334.
[2] Z. Yang, J. Zhang, M.C.W. Kintner-Meyer, X. Lu, D. Choi, J.P. Lemmon, J. Liu, Electrochemical Energy Storage for Green Grid, Chem. Rev. 111 (2011) 3577–3613.
[3] A. Sternberg, A. Bardow, Power-to-What – Environmental Assessment of Energy Storage Systems, Energy Environ. Sci. 8 (2015) 389–400.
[4] H. Sun, Y. Miao, G. Wang, X. Han, Y. Wang, Z. Zhang, C. Luo, X. Liu, C. Xu, H. Chen, Sonochemical synthesis of battery-type $ZnCo_2O_4$ electrode material with huge specific surface area for advanced hybrid supercapacitors, J. *Energy Storage* 76 (2024) 109780.
[5] L.L. Zhang, X.S. Zhao, Carbon-based materials as supercapacitor electrodes, Chem. Soc. Rev. 38 (2009) 2520–2531.
[6] M. Karnan, A.G.K. Raj, K. Subramani, S. Santhoshkumar, M. Sathish, The Fascinating Supercapacitive Performance of Activated Carbon Electrodes with Enhanced Energy Density in Multifarious Electrolytes, Sustainable Energy Fuels 4 (2020) 3029–3041.
[7] S. Suresh Balaji, S. Mohammad Tauquir, M. Karnan, M. Moorthy, M. Sathish, Enhancement in the Specific Energy of B-Doped Graphene Using Redox Additive Electrolytes, ChemistrySelect 5 (2020) 9825–9833.
[8] M. Salaheldeen, T.N.A. Eskander, M. Fathalla, V. Zhukova, J.M. Blanco, J. Gonzalez, Arcady, A.M. Abu-Dief, Empowering the future: cutting-edge developments in supercapacitor technology for enhanced energy storage, Batteries 11 (2025) 232.
[9] U.K. Singh, H. Kaur, P. Kaur, R. Rastogi, Unlocking potential: recent advances in MXene supercapacitors for flexible energy storage devices, Nano-Struct. Nano-Objects 39 (2024) 101290.
[10] S.A. Kadam, K.P. Kadam, N.R. Pradhan, Advancements in 2D MXene-Based Supercapacitor Electrodes: Synthesis, Mechanisms, Electronic Structure Engineering, Flexible Wearable Energy Storage for Real-World Applications, and Future Prospects, J. Mater. Chem. A 12 (2024) 17992–18046.
[11] L. Bai, H. Yin, L. Wu, X. Zhang, First-principle study of the $Nb_{n+1}C_nT_2$ systems as electrode materials for supercapacitors, Comput. Mater. Sci. 143 (2018) 225.
[12] J. Zhu, A. Chroneos, U. Schwingenschlögl, Nb-based MXenes for Li-ion battery applications, Phys. Status Solidi A 9 (2015) 726–729.
[13] M. Arunkumar, K. Nasrin, N. Allwyn, P. Kavinkumar, A. Sivashanmugam, M. Sathish, The emerging heteroepitaxial NiSe2/Nb2C: a two-in-one bi-functional

material architecture for electrocatalytic and supercapattery application, Adv. Sustainable Syst. 8 (2024) 2400088.
[14] Y. Al-Hadeethi, M.W. Iqbal, B.M. Raffah, E. Umar, Synergistic advancements in battery-grade energy storage: Nb2C/MoTe2(PANI) hybrid electrode material as an enhanced electrocatalyst for hydrogen reduction reaction, Electrochim. Acta 508 (2024) 145205.
[15] R. Sukanya, R. Karthik, M. Hasan, C. Breslin, J.J. Shim, Insight into the Synergistic Effect of 2D/2D Layered Metal Selenides Wrapped Nickel Boride Nanoparticles Based Ternary Heterostructure for Constructing Asymmetric Supercapacitors with Excellent Energy Density, Chem. Eng. J. 473 (2023) 145487.
[16] D. Wang, Y. Zhang, J. Chen, H. Xu, L. Qin, Y. Li, W. Zhang, P. Zhang, W. Tian, X. Guo, Z.M. Sun, Structural Hybridization of Ternary (0D, 1D, and 2D) Composites as Anodes for High-Performance Li-Ion Batteries, Energy Storage Mater. 13 (2018) 293–302.
[17] B. Shen, X. Liao, X. Zhang, H.T. Ren, J.-H. Lin, C.-W. Lou, T.T. Li, Synthesis of Nb2C MXene-based 2D layered structure electrode material for high-performance battery-type supercapacitors, Electrochim. Acta 413 (2022) 140144.
[18] R. Sukanya, S.M. Chen, Amorphous Cobalt Boride Nanosheets Anchored Surface-Functionalized Carbon Nanofiber: A Bifunctional and Efficient Catalyst for Electrochemical Sensing and Oxygen Evolution Reaction, J. Colloid Interface Sci. 580 (2020) 318–331.
[19] R. Karthik, R. Sukanya, S.M. Chen, M. Hasan, G. Dhakal, P.M. Shafi, J.J. Shim, Development of an Amorphous Nickel Boride/Manganese Molybdate Heterostructure as an Efficient Electrode Material for a High-Performance Asymmetric Supercapacitor, ACS Appl. Mater. Interfaces 15 (2023) 11927–11939.
[20] T. Li, C. Zhu, X. Yang, Y. Gao, W. He, H. Yue, H. Zhao, Co_3O_4 Nanoneedle@ Electroactive Nickel Boride Membrane Core/Shell Arrays: A Novel Hybrid for Enhanced Capacity, Electrochim. Acta 246 (2017) 226–233.
[21] Y. Chen, T. Zhou, L. Li, W.K. Pang, X. He, Y.-N. Liu, Z. Guo, Interfacial Engineering of Nickel Boride/Metaborate and Its Effect on High Energy Density Asymmetric Supercapacitors, ACS Nano 13 (2019) 9376–9385.
[22] X. Cao, X. Wang, L. Cui, D. Jiang, Y. Zheng, J. Liu, Strongly Coupled Nickel Boride/ Graphene Hybrid as a Novel Electrode Material for Supercapacitors, Chem. Eng. J. 327 (2017) 1085–1092.
[23] R. Sukanya, M. Hasan, R. Karthik, D. Ranjith Kumar, E. Kamaraj, A. Milton, C. Breslin, J. Lee, J.J. Shim, In Situ Decoration of 0D-Nickel Boride on 2D-Vanadium MXene Composites: An Advanced Electrode Material for High Energy Density Supercapacitors, Chem. Eng. J. 497 (2024) 154928.
[24] A. Syed, S.A. Zahra, A. Nasir, M. Yousaf, S. Rizwan, Improved electrocatalytic efficiency of nitrogen-doped Nb2CTx MXene in basic electrolyte for overall water splitting, Int. J. Hydrog. Energy 83 (2024) 39–50.
[25] B. Shen, X. Liao, X. Hu, H.-T. Ren, J.-H. Lin, C.-W. Lou, T.T. Li, A Hollow Nano-Flower $NiCo_2O_4$@Nb_2CT_x MXene Heterostructure via Interfacial Engineering for High-Performance Flexible Supercapacitor Electrodes, J. Mater. Chem. A 11 (2023) 16823.
[26] M. Naguib, J. Halim, J. Lu, K.M. Cook, L. Hultman, Y. Gogotsi, M.W. Barsoum, New Two-Dimensional Niobium and Vanadium Carbides as Promising Materials for Li-Ion Batteries, J. Am. Chem. Soc. 135 (2013) 15966–15969.
[27] J. Halim, K.M. Cook, M. Naguib, P. Eklund, Y. Gogotsi, J. Rosen, M.W. Barsoum, X-Ray Photoelectron Spectroscopy of Select Multi-Layered Transition Metal Carbides (MXenes), Appl. Surf. Sci. 362 (2016) 406–417.
[28] D. Briggs, in: C.D. Wanger, W.M. Riggs, L.E. Davis, J.F. Moulder, G.E. Muilenberg (Eds.), Handbook of X-Ray Photoelectron Spectroscopy, Perkin-Elmer, Eden Prairie, MN, 1979.
[29] G. Gouget, D.P. Debecker, A. Kim, G. Olivieri, J.J. Gallet, F. Bournel, C. Thomas, O. Ersen, S. Moldovan, C. Sanchez, S. Carenco, D. Portehault, In Situ Solid-Gas Reactivity of Nanoscaled Metal Borides from Molten Salt Synthesis, Inorg. Chem. 56 (2017) 9225–9234.
[30] J. Xiao, J. Wen, J. Zhao, X. Ma, H. Gao, X. Zhang, A safe etching route to synthesize highly crystalline Nb2CTx MXene for high-performance asymmetric supercapacitor applications, Electrochim. Acta 337 (2020) 135803.
[31] Y. Yamada, Y. Iriyama, T. Abe, Z. Ogumi, Kinetics of Lithium-Ion Transfer at the Interface between Graphite and Liquid Electrolytes: Effects of Solvent and Surface Film, Langmuir 25 (2009) 12766–12770.
[32] S.Y. Vassiliev, V.V. Sentyurin, E.E. Levin, V.A. Nikitina, Diagnostics of Lithium-Ion Intercalation Rate-Determining Step: Distinguishing between Slow Desolvation and Slow Charge Transfer, Electrochim. Acta 302 (2019) 316–326.
[33] Y. Lu, J. Liang, S. Deng, Q. He, S. Deng, Y. Hu, D. Wang, Hyper crosslinked polymers enabled micropore-dominant N,S co-doped porous carbon for ultrafast electron/ion transport supercapacitors, Nano Energy 65 (2019) 103993.
[34] S. Guan, X. Fu, B. Zhang, M. Lei, Z. Peng, Cation-Exchange-Assisted Formation of NiS/SnS_2 Porous Nanowalls with Ultrahigh Energy Density for Battery-Supercapacitor Hybrid Devices, J. Mater. Chem. A 8 (2020) 3300–3310.
[35] M.R. Lukatskaya, O. Mashtalir, C.E. Ren, Y. Dall'Agnese, P. Rozier, P.L. Taberna, M. Naguib, P. Simon, M.W. Barsoum, Y. Gogotsi, Cation intercalation and high volumetric capacitance of two-dimensional titanium carbide, Science 341 (2013) 1502–1505.
[36] P. Barmann, M. Winter, J.G. Julian, T. Placke, Solvent co-intercalation-induced activation and capacity fade mechanism of few−/multi-layered MXenes in lithium-ion batteries, Small 17 (2021) 2104130.
[37] X. Liu, W. Xu, D. Zheng, Z. Li, Y. Zeng, X. Lu, Carbon cloth as an advanced electrode material for supercapacitors: Progress and challenges, J. Mater. Chem. A 8 (2020) 17938.
[38] H. Aydın, U. Kurtan, B. UstUn, S.N. Koc, E. Akgul, M. De, A review on the recent advancement of metal-boride derived nanostructures for supercapacitors, J. Energy Storage 72 (2023) 108306.
[39] U. Ahmed, G. Nabi, Nonhazardous in-situ exfoliation approach for Ta-Nb_2CT_x MXenes as sustainable supercapacitor electrode applications, J. Power Sources 653 (2025) 237745.
[40] U. Ahmed, G. Nabi, Nonhazardous in-situ exfoliation approach for Ce-Nb_2CT_x MXene as highly stable pseudocapacitors electrode material applications, J. Environ. Chem. Eng. 13 (2025) 115949.
[41] F.N.T. Yesilbag, Y.O. Yesilbag, A. Huseyin, A.J.S. Salih, M. Ertugrul, Ti2NbC2Tx MXene nanosheets as an ordered double transition metal electrode for high-performance supercapacitors, ACS Appl. Nano Mater. 8 (2025) 9211–9226.
[42] K.A. Rao, M.E. Mazhar, J. Ahmad, M. Bilal, M.I. Khan, M.S. Ahmad, M. Aziz, H. Rehman, Nb_2CT_x MXene integrated $DyMn_2O_5$ composites: tailored particle size and enhanced capacitance for high performance pseudocapacitors, J. Mater. Chem. C 13 (2025) 13803.
[43] Shavita, K.K. Thakur, A.L. Sharma, S. Singh, Exploring MXene-MOF composite for supercapacitor application, Mater. Chem. Phys. 322 (2024) 129463.
[44] B. Shen, X. Hu, H.T. Ren, H.K. Peng, B.C. Shiu, J.H. Lin, C.W. Lou, T.T. Li, Rosette-like (Ni,Co)Se_2@Nb_2CT_x MXene heterostructure with abundant Se vacancies for high-performance flexible supercapacitor electrodes, Chem. Eng. J. 484 (2024) 149440.
[45] R. Sukanya, R. Karthik, A. Al Mahmud, E. Dempsey, D.R. Kumar, C.B. Breslin, J. J. Shim, Rational design of interface-coupled Nb-doped $MoSe_2/Nb_2CT_x$ MXene heterostructures with enriched active sites toward enhanced hydrogen evolution reaction, J. Power Sources 673 (2026) 239674.